

NATIONAL UNIVERSITY OF SINGAPORE

CENTRE FOR QUANTUM TECHNOLOGIES

**Characterization of Single-Photon
Detectors with Tightly Time-Correlated
Photon Pairs**

Author:

Antony Winata

HARTANTO

Supervisor:

Professor Christian

KURTSIEFER

Report submitted in partial fulfilment for the module

PC3288 Advanced UROPS in Physics I

in the

Department of Physics

National University of Singapore

May, 2020

Acknowledgements

First and foremost, I would like to express my sincerest gratitude to my postdoc, Shen Lijiong, for guiding me through many aspects of the experiment, patiently explaining every little thing I am curious about (experiment-related or otherwise). Without him, I would be in a limbo, not knowing what is going on in the experiment. Thank you for showing me the ropes on how to write a good report, and spending some time to give constructive feedback on my drafts.

Next, I would like to thank my supervisor, Prof. Christian Kurtsiefer, for giving me the opportunity to work with the amazing Quantum Optics group and on this project. Thank you for all the insightful discussions during the weekly group meeting and during the DYOM module. You inspire me to be a scientist that is able to not "only" do science but also engineer what is needed to do that science.

Special thanks to my other postdoc, Lee Jianwei, for answering all my trivial questions and helping me improve my report drafts.

Last but definitely not least, thank you to each and everyone in the Quantum Optics group for the awesome learning experience!

Abstract

The instrument response function (IRF) is an important characteristic of an SPD that can be used to describe the timing jitter of a single-photon detector (SPD). In applications involving time-resolved measurements, any cause of timing uncertainty needs to be taken into account to arrive at a more precise measurement of the physical quantity of interest. In this report, the IRF and timing jitter of three different types of SPDs are characterized. We characterize the thin silicon single-photon avalanche detector (SPAD) over the visible band, the indium gallium arsenide (InGaAs) SPAD over the telecommunications band, and the superconducting nanowire single-photon detector (SNSPD) over the visible and telecommunications band.

The IRF is determined through the cross-correlation between the detection times recorded with an unknown and a reference detector, while the timing jitter was determined by taking the full-width half-maximum (FWHM) of the IRF. The characterization is done using tightly time-correlated photon pairs generated in spontaneous parametric down-conversion (SPDC) instead of a typical pulsed laser system. The source is tunable over a range of wavelength comparable to that of existing pulsed-laser systems.

Contents

Acknowledgements	iii
Abstract	v
1 Introduction	1
2 Theory and Background	3
2.1 Detection of Light at Single-Photon Level	3
2.1.1 Introduction to Photodiode and Avalanche Photodiode	4
2.1.2 Thin SPAD	6
2.1.3 InGaAs SPAD	8
2.2 Superconducting Nanowire Single-Photon Detector	9
3 Timing jitter characterization	11
3.1 Tightly Time-Correlated Photon Pair Source	11
3.2 Experiment set-up	13
3.2.1 Characterizing SNSPD	13
PPKTP-based source with 405 nm laser diode	14
PPKTP-based source with 532 nm laser diode	15
BBO-based source with 405 nm laser diode	16
3.3 Characterization of Detector Instrument Response Function .	18
3.4 Characterizing Timing Jitter of SNSPD	18
3.5 Characterizing Timing Jitter of thin SPAD	21

3.6	Characterizing Timing Jitter of InGaAs SPAD	26
4	Conclusion	29
	Bibliography	31

List of Figures

2.1	A simplified illustration of a p-n junction, formed by an n-type and p-type semiconductor material	5
2.2	A cross-section of a thin SPAD	7
2.3	A cross-section of an InGaAs SPAD	8
2.4	A schematic of the working principle of an SNSPD.	10
3.1	Experiment set-up with PPKTP-based source pumped with a 405 nm laser diode	14
3.2	Experiment set-up with PPKTP-based source pumped with a 532 nm laser diode	16
3.3	Experiment set-up with BBO-based source pumped with a 405 nm laser diode	17
3.4	Cross-correlation function between two degenerate 810 nm photon-pairs detected using two SNSPDs	19
3.5	Cross-correlation function between 810 nm and 1550 nm photon-pairs detected using two SNSPDs	20
3.6	Cross-correlation function between 548 nm and 1550 nm photon-pairs detected using two SNSPDs	21
3.7	Cross-correlation function between two photon pairs detected using thin SPAD and SNSPD	22
3.8	The characteristic time constant of the exponential component in the IRF of a thin SPAD	24

3.9	Variation in the characteristic timing jitter of a thin SPAD at different photon wavelengths	25
3.10	Cross-correlation function between two photon pairs detected using InGaAs SPAD and SNSPD	26
3.11	Characteristic timing jitter of an InGaAs SPAD at different photon wavelengths	28

Chapter 1

Introduction

Single-photon detectors (SPDs) are used for the detection of light at the single-photon level. Some applications of SPDs include quantum communications, photon-pair correlation measurements, and fluorescence lifetime measurements [1–3]. These applications typically involve time-resolved measurements. Depending on the application, a certain type of SPD is preferred due to it having more suitable characteristics for that particular application. These characteristics are the IRF and the timing jitter of the detector.

The timing jitter is the statistical fluctuation of the time interval between the arrival of a photon on the detector and the output signal produced by the detector [2, 4]. To measure timing jitter, one dependable method is by taking the full-width half-maximum (FWHM) of the IRF [2]. In applications involving time-resolved measurements, sources of timing uncertainty needed to be taken into account to arrive at a more precise measurement. Hence, the characterization of the timing jitter of the SPD is important.

Typically, the IRF of a detector is obtained from the arrival time distribution of photons collected from a pulsed laser. In this report, we use alternative sources that generate tight timing-correlated photon pairs via

spontaneous parametric down-conversion (SPDC). The tight timing-correlation, typically around the order of hundreds of femtoseconds, can be used to infer the IRF through the cross-correlation function between the photon pairs detected by the detectors. The sources used do not require the construction of an optical cavity, is relatively easy to align and is capable of producing photon-pairs at a range comparable to existing pulsed laser systems [5]

The outline of this report is as follows: in Chapter 2, we introduce and provide an overview of the principle behind the SPDs. The SPDs explored in this report are the superconducting nanowire single-photon detector (SNSPD) from Single Quantum (SSPD-1550Ag), a thin silicon Single-Photon Avalanche Diode (SPAD) from Micro Photon Devices (PD-050-CTC-FC), and an indium gallium arsenide (InGaAs) SPAD from S-Fifteen Instruments (ISPD1). In Chapter 3, we outline and explain briefly the principle behind SPDC and the three photon-pair sources used in the experiment. Afterward, we discuss the timing jitter characterization of the SPDs and the device physics behind the results. Finally, in Chapter 4, we will conclude with a summary of the detector characterizations and its implications.

Chapter 2

Theory and Background

2.1 Detection of Light at Single-Photon Level

The detection of light in discrete energy quanta was first made possible by the invention of the photoelectric tube by Elster and Geiger in 1913 [6]. This invention made use of the photoelectric effect where light of certain frequency incident on a surface of metal would cause the electron on the surface of the metal to be liberated. The effect, which is independent of intensity and is dependent only on the frequency of the incident light, was postulated by Albert Einstein in 1905 [7]. Later on, the development of the photomultiplier tube (PMT) would mark the first milestone of detection of light at a single-photon level [6]. As photons pass through the window of the PMT and hit the surface of metal called the photocathode, photoelectrons are emitted due to the photoelectric effect. These photoelectrons are accelerated towards a series of materials that act as electron multipliers called the dynodes. Here electrons would be multiplied through secondary emission. These electrons would then be directed towards and detected at the anode [8].

From past experimental measurements, the timing jitter of PMTs is determined to be in the order of hundreds of picoseconds [2, 8]. This timing

jitter is comparable to some types of SPDs such as the visible-light photon counters or a thick silicon SPAD. However, PMTs typically have high dark counts-registered photon counts observed in the absence of incident light [2]. This limits the applicability of PMT in many time-resolved applications. The development of SPDs then shifted to the use of solid-state semiconductors as photodetectors. These semiconductor photodetectors, also known as photodiodes, utilize the presence of a p-n junction in the semiconductor material [6].

2.1.1 Introduction to Photodiode and Avalanche

Photodiode

A photodiode is a semiconductor device that absorbs incoming photons to excite valence band electrons (holes) to conduction band electrons (holes). This is possible through manipulating the electronic properties of semiconductor materials, typically silicon (Si), germanium (Ge), and gallium arsenide (GaAs), by the addition of impurities (also known as doping). Doped semiconductors that contain excess holes are referred to as 'p-type' while those that contain excess free electrons are known as 'n-type' [9].

A p-n junction is formed when p-type and n-type semiconductors are joined together due to the diffusion of charge carriers. Electrons from the n-type region would diffuse towards the p-type region while holes from the p-type region would diffuse towards the n-type region. These diffused electrons and holes would recombine at the junction to form the depletion region. The charge polarity between the n-type and p-type regions would also simultaneously create a potential difference across the depletion region, generating an electric field as shown in Fig. 2.1.

When photons with energy greater than the bandgap of the semiconductor used in the photodiode, they have a higher probability of

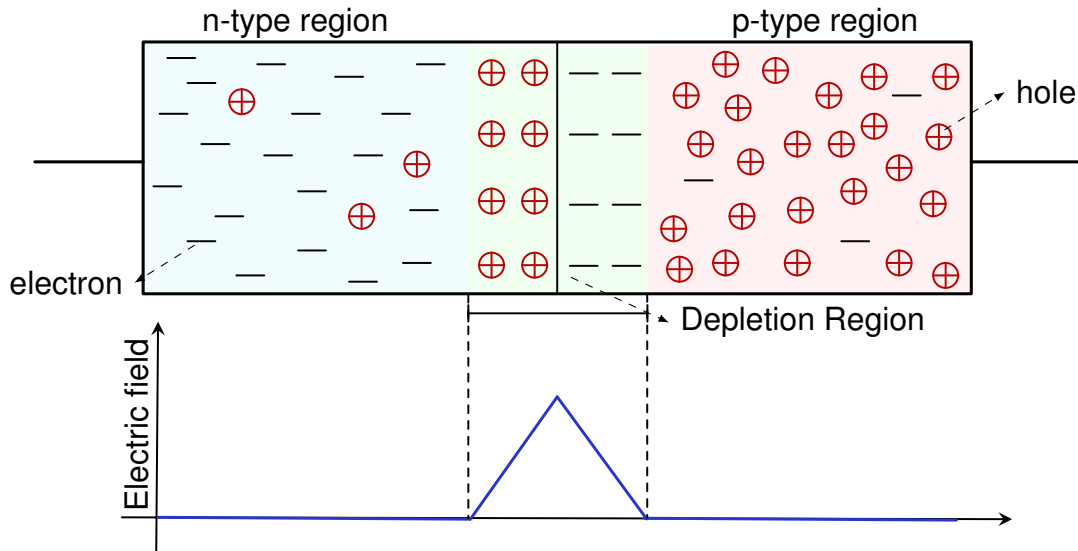


FIG. 2.1. A simplified illustration of a p-n junction, formed by an n-type and p-type semiconductor material. A region called the depletion region is formed at the junction between the two types of semiconductors due to the recombination of holes and electrons. A qualitative electric field profile denotes the regions with a high electric field.

being absorbed. The absorption of photons generates an electron-hole pair as free charge carriers in the process. The generated electrons and holes are then accelerated by the electric field formed due to the charge separation in the depletion region. As a result of the movement of these charge carriers, a flow of electrons is created through the photodiode. Application of a reverse bias voltage, where negative bias is applied at the p-type region while positive bias is applied at the n-type region, can further increase the electric field strength across the depletion region. This would allow the created charge carriers to move at a greater velocity out of the depletion region and create a larger photocurrent.

To allow a photodiode to have a higher detection probability, a larger photon absorbing region is required. This can be done by adding an intrinsic (undoped) region between the two doped regions, creating a PIN junction. The intrinsic region serves to increase the area where electron-hole pairs can be created. This would result in a higher probability of each photon forming charge carriers, resulting in higher photon detection efficiency or the

probability that the detector would register an output signal when a photon arrives at the detector [2].

The application of high reverse bias voltage would enable the PIN photodiode to detect low-intensity light down to a single-photon level. This is because the application of high reverse bias would create a greater electric field in the intrinsic region where charge carriers are formed. The free charge carriers can then gain greater kinetic energy which allows them to produce secondary charge carriers through impact ionization, leading to an avalanche. Thus, this kind of photodiode is also known as an avalanche photodiode (APD). One commonly used APD is the silicon APD (Si APD). The bandgap of silicon is approximately 1.12 eV, making the Si APDs sensitive to photons with wavelengths ranging from 150 nm to 1100 nm [9].

One mode of detector operation used to detect single-photons is the Geiger-mode APD [9]. For this report, we will be referring to Geiger-mode APD more straightforwardly as a Single-Photon Avalanche Diode (SPAD). The operating principle of a SPAD is based on reverse-biasing the PIN junction at a voltage higher than the breakdown voltage of the junction. In this mode, the electric field is sufficient to cause a single charge carrier to trigger a self-sustaining avalanche. The predominant source of noise for SPADs is due to thermal or field-related components in the absence of incoming photons [1]. Knowing this allows further development in the detector device structure to minimize the noise in the SPAD.

2.1.2 Thin SPAD

Generally, the depletion region of a silicon SPAD can be up to 25 μm in thickness. Such SPAD has relatively good photon detection efficiency and low noise. However, it has a large timing jitter in the order of a few hundreds of picoseconds [10]. To improve upon this, a silicon SPAD with a thinner

depletion region was designed. This silicon SPAD has a depletion region of about 1 - 2 μm and is dubbed thin SPAD in this report. The thin SPAD has low dark count and attained timing jitter as low as 30 ps [10]. To achieve these characteristics, a double-epitaxy structure is used to reduce the drift effect of the charge carriers through the sharp increase in the electric field at the active region [10]. Figure. 2.2 illustrates a cross-section of the thin SPAD.

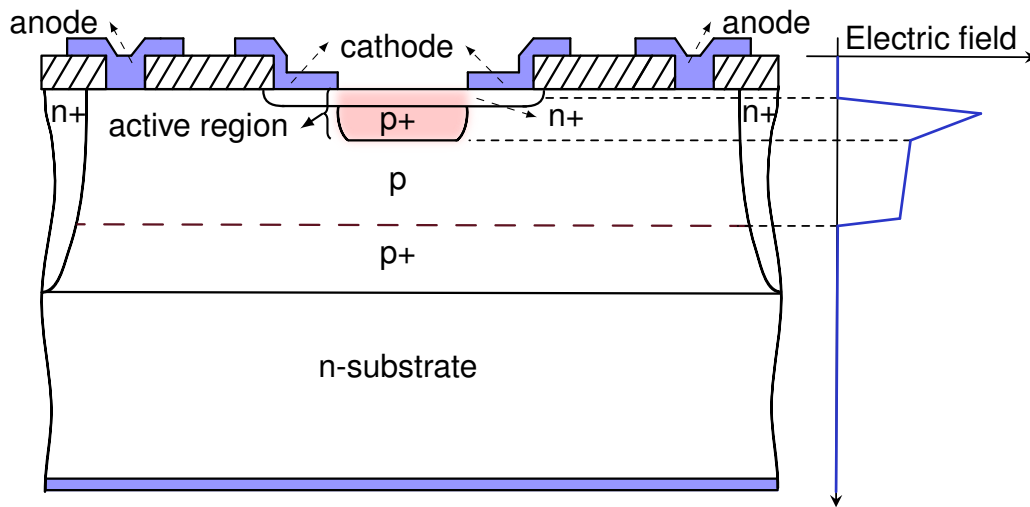


FIG. 2.2. A cross-section of a thin SPAD. Boron-implanted n+ and p+ doped junction forms an active region with a high electric field, contributing to the low timing jitter of the device. A qualitative electric field profile denotes the regions with a high electric field [10, 11].

A boron-implanted part of the n+ and p+ doped junction gives rise to a high electric field region, making it the part of the SPAD that is active in producing photoelectrons [11]. This high electric field partly enables the device to achieve low timing jitter. The active region is fabricated on top of the p doped layer, which is followed by the highly doped p+ layer that presents a low-resistance path for the produced charge carriers. This would allow charge carriers to flow faster after being created. Electrical insulation from the adjacent SPADs to prevent current leakage is ensured by integrating highly doped n+ regions with the n-doped region in the device [10].

In the case of a thin SPAD, the timing jitter is mainly contributed from the process of absorption of a photon to produce charge carriers or motion of

the charge carrier in the intrinsic region of the semiconductor. This timing jitter is typically in the order of tens of picoseconds [10]. Having low timing jitter is crucial especially in high precision time-resolved measurements as it decreases the timing uncertainties of the measured correlation.

2.1.3 InGaAs SPAD

Indium gallium arsenide (InGaAs) SPAD is a group III-IV heterostructure device and is used primarily for single-photon detection in the infrared to the near-infrared regime. It is a type of APD with different structure and dopant to allow for optimized detection efficiency in the desired wavelengths. Figure 2.3 shows a cross-section of the InGaAs SPAD. An InGaAs layer works as the absorption region in the device, with a bandgap of 0.75 eV. Another lattice-matched InP layer, on the other hand, forms a multiplication layer that generates secondary electrons via impact ionization in the device. At this multiplication layer, the high electric field formed by applying bias voltage above the detector breakdown voltage to increase the likelihood of avalanche where secondary electrons exponentially produce more electrons [1].

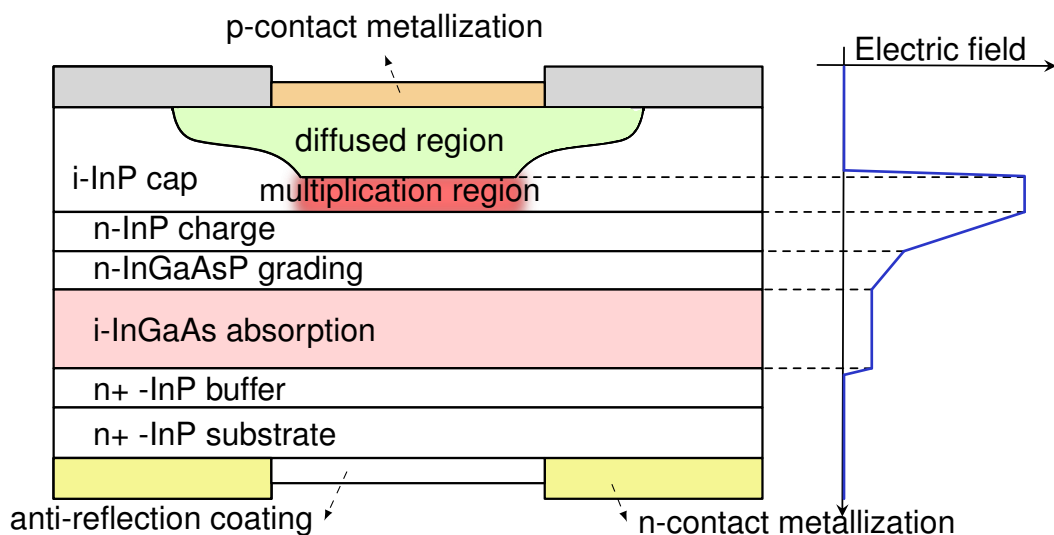


FIG. 2.3. A cross-section of an InGaAs SPAD. A qualitative electric field profile denotes the regions with a high electric field [1].

Photons incident on the detector will be absorbed in the absorption region, forming free electron-hole pair as charge carriers. The electric field in the region would cause the charge carriers to move towards the multiplication layer where the high electric field in that layer led to the formation of a self-sustaining avalanche. This would then be detected as a surge in current in the circuit, indicating the detection of a single photon. Depending on the bias voltage, the timing jitter of InGaAs SPADs can be in the order of hundreds of picoseconds [1, 2].

2.2 Superconducting Nanowire Single-Photon Detector

The superconducting nanowire single-photon detector (SNSPD) detects photons through a state transition that occurs when the detector absorbs a photon. Coupled with advances in micro-fabrication techniques and cooling technologies, SNSPD began to take hold as one of the most temporally precise detectors. SNSPD has great potential in time-correlated single-photon applications due to its fast recovery time and timing precision [12]. One type of material often regarded as a first choice for the nanowire in the SNSPD is niobium nitride (NbN) due to its relative ease of fabrication and good sensitivity over a wide range of wavelengths [12]. The SNSPD works using the following principles as outlined in Fig. 2.4.

The NbN SNSPD is direct current biased below its critical current. A photon incident on the nanowire detector has sufficient energy to cause a state transition, forming a hotspot. Such hotspot has a low probability of forming in absence of an incident photon, allowing SNSPD to have exceptionally low dark count [13]. The formation of a hotspot would lead to an increase in the local current density in the surrounding region (where the

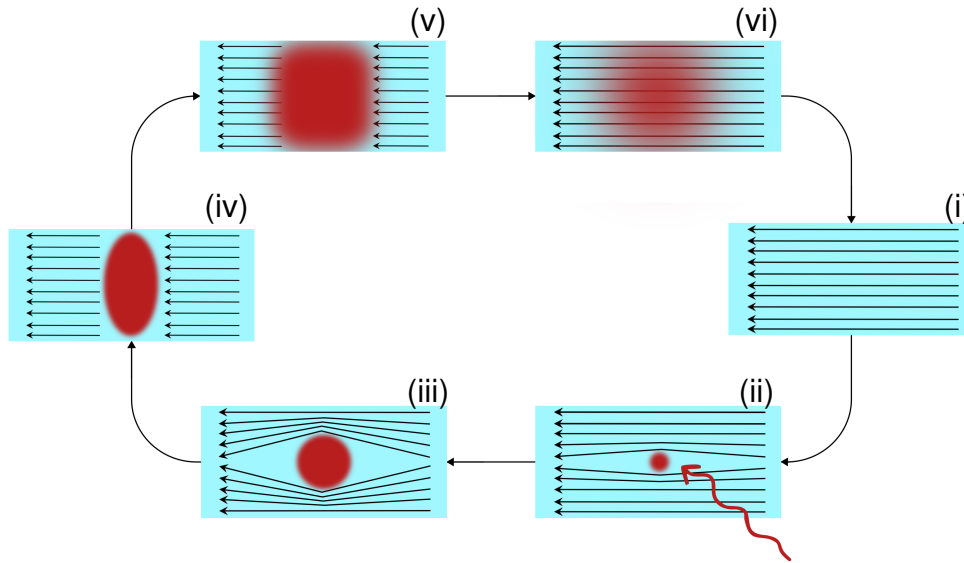


FIG. 2.4. A schematic of the working principle of an SNSPD [12]. (i) The nanowire is maintained below the superconducting critical temperature and is direct current (DC) biased below its critical current. (ii) A photon incident on the nanowire is absorbed and led to the creation of a small resistive hotspot on the nanowire. (iii) The resistive hotspot causes the current to flow around it. Local current density around the hotspot increases until it exceeds the critical current density due to the narrowness of the nanowires. (iv) As a result, a resistive barrier is formed across the width of the nanowire [13]. (v) The DC bias also led to joule heating, furthering the growth of the resistive region along the nanowire axis to the point where current stops flowing [14]. The biased DC would also be shunted by the external circuit. (vi) This allows the dispersion of the resistive region and returns the nanowire to its superconducting state again. The biased DC is then returned to the original value.

hotspot has not formed) due to the increase in the size of the hotspot. When the superconducting current density reaches its critical value, the nanowire loses its superconductivity, where it has zero resistance, and regain its normal-state resistance. This would eventually lead to a resistive barrier along the width of the nanowire, generating a measurable output voltage across the nanowire [13].

The timing jitter of an SNSPD is can be in the order of picoseconds to tens of picoseconds depending on the size and geometry of the nanowire [12, 15]. This level of timing jitter is, comparable to that of a thin SPAD and actively quenched SPAD [2, 16].

Chapter 3

Timing jitter characterization

Characterization of detectors used is a crucial step in determining the suitability of the detectors for the intended application. For instance, the timing jitter of a detector would have a direct influence on the precision of timing measurements. Low detector timing jitter is generally required in time-resolved measurements, for example in single-photon quantum communication or time-resolved correlation spectroscopy [17–19]. In this chapter, we perform a quantitative characterization of timing jitter of SNSPD and two variants of SPADs.

3.1 Tightly Time-Correlated Photon Pair Source

To characterize the SPDs, we distribute time-correlated photon pairs generated through spontaneous parametric down-conversion (SPDC) to two SPDs. Due to the tight-timing correlations (in the order of a few hundred femtoseconds) between each photon in the pair, the probability distribution of the detection time differences between the two SPDs will be governed mainly by the timing jitter of the SPDs [20]. In this report, we use three different sources based on SPDC. Two sources are produced using a

periodically poled potassium titanyl phosphate (PPKTP) crystal ($2 \times 1 \times 10 \text{ mm}^3$) and one source using a β -Barium Borate (BBO) crystal ($2 \times 2 \times 2 \text{ mm}^3$) [21–25].

PPKTP crystal produces photon pairs using photons from a pump source through a nonlinear interaction in a the periodically poled crystal [26–28]. The produced photon pairs are traditionally referred to as the signal and idler photons. The produced photon pairs must satisfy energy and momentum conservation as follows

$$\omega_p = \omega_s + \omega_i, \quad (3.1)$$

and

$$\vec{k}_p = \vec{k}_s + \vec{k}_i, \quad (3.2)$$

where ω_p and \vec{k}_p denote the frequency and momentum of the pump photons respectively, ω_s and \vec{k}_s denote the frequency and momentum of the signal photons respectively, and ω_i and \vec{k}_i denote the frequency and momentum of the idler photons respectively. These are the phase-matching condition for SPDC. In the case of a periodically poled crystal, such as a PPKTP crystal, there is an additional term in the momentum conservation to satisfy the quasi-phase-matching condition:

$$\vec{k}_p = \vec{k}_s + \vec{k}_i + \frac{2\pi}{\Lambda}, \quad (3.3)$$

where Λ is the poling period of the poled nonlinear crystal. The PPKTP crystal we used in the experiment has a poling period of $9.64 \mu\text{m}$, allowing the generation of 810 nm degenerate photon pairs as well as 810 nm and 1550 nm non-degenerate photon pairs depending on the pump wavelength used.

BBO crystal produces photon pairs through phase matching interaction

of SPDC [21–24]. Thus, the signal, idler and pump photons must obey the energy and momentum conservation shown in Eqn. 3.1 and Eqn. 3.2 respectively. With a BBO crystal, it is possible to achieve critical phase-matching by angle tuning, allowing the generation of idler and signal photons of various wavelengths [29, 30].

3.2 Experiment set-up

Different photon wavelength produced by the photon sources requires a corresponding optical component in the experimental set-up to optimize the photon counts incident on the detector. To characterize the SNSPD at 548 nm, 810 nm, and 1550 nm, we use two photon-pair sources produced by the PPKTP crystal and one photon-pair source by the BBO crystal. Subsequently, the characterization of thin SPAD and InGaAs SPAD is also done using photon-pairs produced by the BBO crystal. The choice of using PPKTP as the photon pair source to characterize the SNSPD was due to convenience as there is a pre-existing PPKTP-based source in the lab rather than a limitation in the BBO crystal in producing photons of the desired wavelengths.

3.2.1 Characterizing SNSPD

The reference detector, SNSPD, is characterized at 548 nm, 810 nm, and 1550 nm. The cross-correlation of the photon detection times at two similar SNSPDs (at SPD-1 and SPD-2) is subsequently used to characterize the instrument response function (IRF) of the detector. The method of characterization and the significance of the IRF will be explored in Section 3.3.

PPKTP-based source with 405 nm laser diode

To characterize the timing jitter of SNSPD at 810 nm, we produce degenerate 810 nm photon pairs using PPKTP-based source pumped with a 405 nm laser diode [25]. A schematic of the experimental set-up is shown in Fig. 3.1.

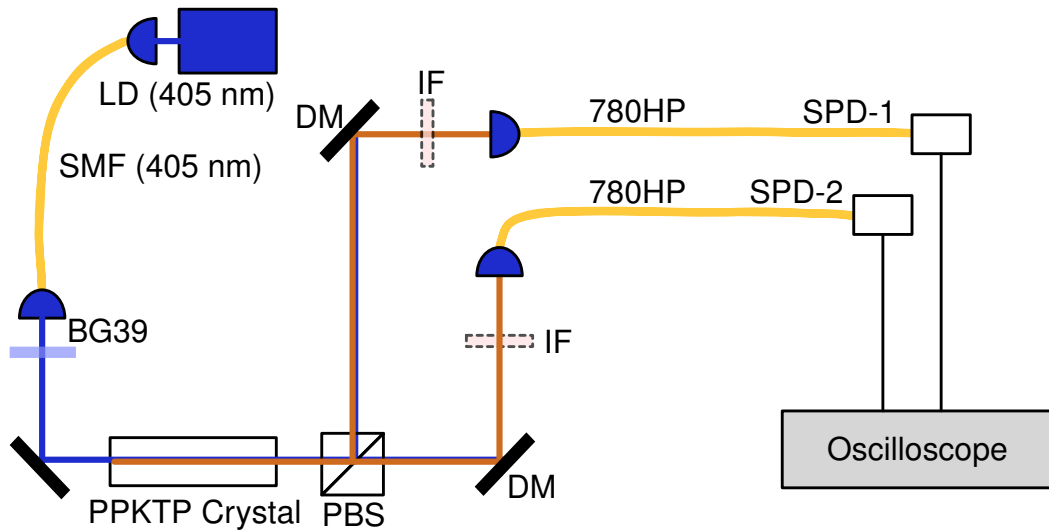


FIG. 3.1. Experiment set-up with PPKTP-based source pumped with a 405 nm laser diode. Light from a laser diode (LD), with wavelength 405 nm was coupled into single-mode fiber (SMF) and directed towards a PPKTP crystal. This produces 810 nm signal and idler photons, which is then split by a polarizing beam splitter (PBS). The split beams are each coupled into an SMF (780HP), before being detected at SPD-1 and SPD-2. In this set-up, both SPD-1 and SPD-2 are SNSPDs. LD: laser diode, PPKTP: periodically poled potassium titanyl phosphate, BG39: blue colored glass bandpass filter, DM: dichroic mirror, IF: 810 nm interference bandpass filter.

The 10 mW pump laser diode is coupled to a single-mode optical fiber to filter the spatial mode and focus it to produce a beam waist of $350 \mu\text{m}$. The focused beam was passed through a blue colored glass band-pass filter (BG39) to filter out broadband fluorescence from the pump laser diode.

Subsequently, the beam is directed into the PPKTP crystal ($9.64 \mu\text{m}$ poling period) which produces tightly time-correlated signal and idler photons. Dichroic mirrors are used to reflect the incident 810 nm photons at a 90° angle to its incident path. The signal and idler photons are then split using a polarizing beam splitter (PBS) into two beams, each passing through

an interference bandpass filter (FF01-810/10-25). These photons are then collected using two collection modes, each with a beam waist of approximately $150\ \mu\text{m}$, defined by the single-mode fiber (SMF). The SMFs (780HP) then deliver the photons to the SNSPDs, where they will be detected.

The arrival time of each photon is registered as the time when the detector signal goes above a threshold. The threshold was set at approximately half of the average signal amplitude observed in an oscilloscope for a single photon event. The cross-correlation events are obtained using a histogram of the detection times registered by SPD-1 measured with an oscilloscope that is triggered by the detection of a photon by SPD-2. The timing jitter of the oscilloscope is approximately $4.4\ \text{ps}$, which is negligible compared to the expected timing jitter of the SPDs that are being characterized. The whole process allows the characterization of the IRF and timing jitter of the SNSPD at $810\ \text{nm}$ described in Section 3.4.

PPKTP-based source with 532 nm laser diode

Next, the pump laser diode in the PPKTP-based source is replaced with a $532\ \text{nm}$ laser diode. This produces non-degenerate photon pairs at $810\ \text{nm}$ and $1550\ \text{nm}$. A schematic of the experimental set-up is shown in Fig. 3.2.

Change in the wavelength of the pump laser diode to $532\ \text{nm}$ produces tightly time-correlated non-degenerate signal and idler photons at $1550\ \text{nm}$ and $810\ \text{nm}$ respectively. The photon pairs are separated using a $100\ \mu\text{m}$ -thick Si wafer with an approximate transmission of 50% for photons in the infrared spectrum (cut-off wavelength, $\lambda_c \approx 1050\ \text{nm}$) but almost zero in the visible spectrum. As such, the Si wafer would allow the signal photons to pass through while the idler photons will be reflected.

Signal photons are coupled into an SMF (SM28e) while the idler photons will be coupled into another SMF (780HP). These photons will then be

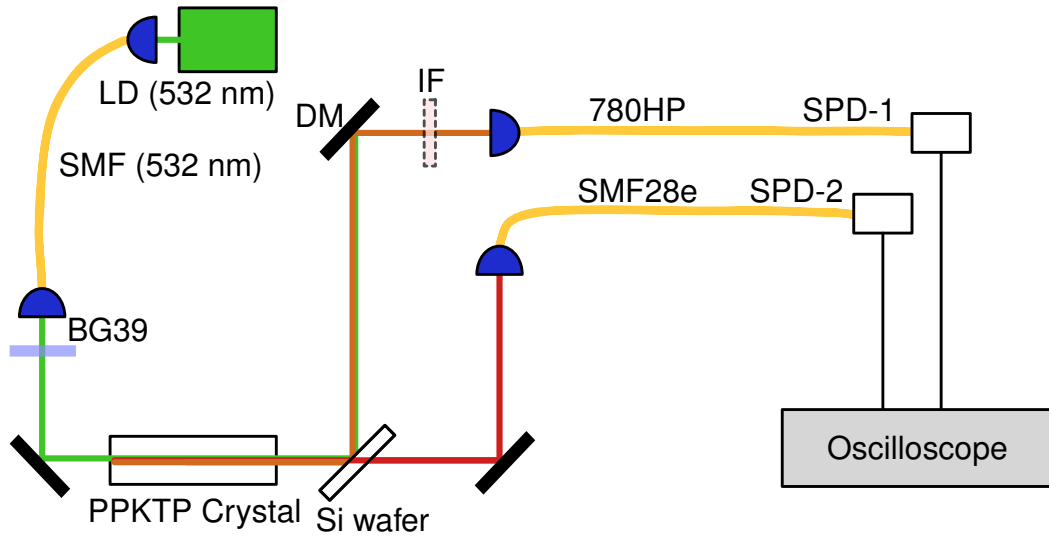


FIG. 3.2. Experiment set-up with PPKTP-based source pumped with a 532 nm laser diode. Light from a laser diode (LD), with wavelength 532 nm was coupled into an SMF and directed towards a PPKTP crystal. This produces 1550 nm signal photons and 810 nm idler photons. A silicon (Si) wafer was placed to separate the photons by the wavelength of each pair. Signal photons are coupled into an SMF (SMF28e), before being detected at SPD-2. Idler photons are coupled into another SMF (780HP), before being detected at SPD-1. In this set-up, both SPD-1 and SPD-2 are SNSPDs. LD: laser diode, PPKTP: periodically poled potassium titanyl phosphate, BG39: blue colored glass bandpass filter, DM: dichroic mirror, IF: 810 nm interference bandpass filter.

delivered into their respective SPDs where the cross-correlation between the arrival times can be obtained.

BBO-based source with 405 nm laser diode

Finally, the pump laser diode in the PPKTP-based source is replaced with a 405 nm laser diode and the photon pair source is replaced with a BBO crystal. This produces non-degenerate photon pairs at 548 nm and 1550 nm. Furthermore, the angle between the BBO crystal and the pump beam can be tuned to vary the wavelengths of the signal and idler photons. A schematic of the experimental set-up is shown in Fig. 3.3.

Separation of the signal and idler photons was done with the Si wafer. One SMF (SM600) collects the signal photons and delivers them to SPD-1

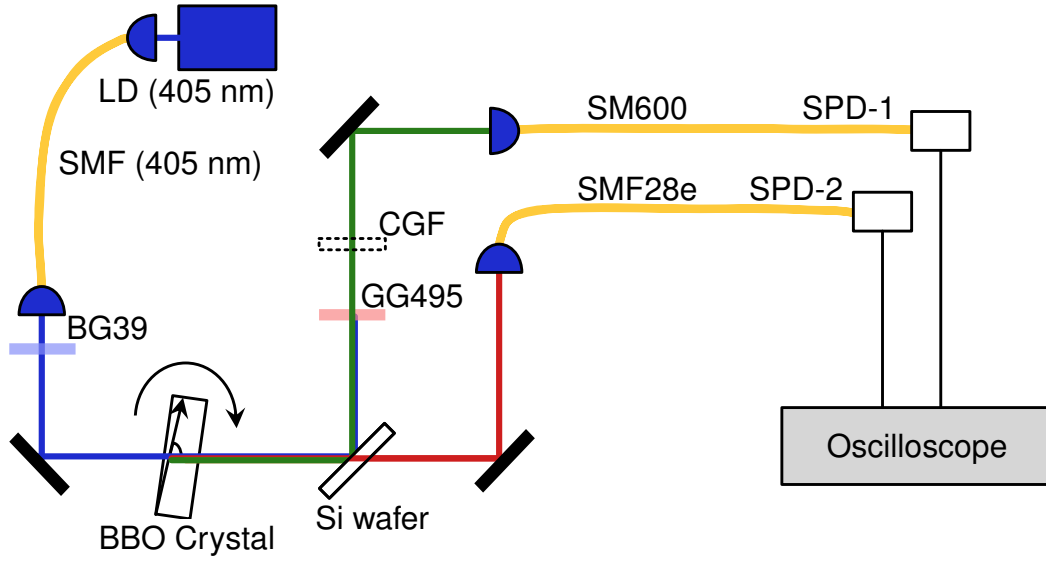


FIG. 3.3. Experiment set-up with BBO-based source pumped with a 405 nm laser diode. Light from a laser diode (LD), with wavelength 405 nm was coupled into single-mode fiber and directed towards a β -Barium Borate (BBO) crystal. The wavelength of the signal and idler photons produced can be tuned by varying angle ϕ of the crystal. A silicon (Si) wafer was placed to separate the photons by the frequency in each pair. A calibrated color glass long-pass filter (CGF) was used to determine the wavelength of the signal photons. Signal photons are coupled into an SMF (SM600), before being detected at SPD-1. Idler photons are coupled into another SMF (SMF28e), before being detected at SPD-2. LD: laser diode, BBO: β -Barium Borate, BG39: blue colored glass bandpass filter, GG495: green colored glass long-pass filter.

while the other SMF (SMF28e) collects idler photons and delivers them to SPD-2.

Determination of the wavelength of the signal photons, λ_s was done by measuring the transmission, T , of the photons through a color glass filter (CGF). Pair source rate detected before and after inserting the filter in the signal path was compared. The change in pair source rate due to the change in T was noted down and checked against a calibration table that relates λ_s and T to determine the signal wavelength [31]. Idler wavelength, λ_i , can then be inferred by invoking Eqn.3.1 together with the measured λ_s and the known pump wavelength, λ_p . This set-up allows SPDs to be characterized for a range of wavelengths as λ_s can range from 526 nm to 661 nm while λ_i ranges from 1050 nm to 1760 nm. The range of wavelengths is

comparable to that found in existing dye and solid-state femtosecond pulsed lasers with the advantage of not requiring any optical cavity and is relatively straightforward to align [5, 32, 33]

3.3 Characterization of Detector Instrument Response Function

To determine the instrument response function (IRF) of a particular detector (i.e. SPD-1), we obtain the cross-correlation function, $g^{(2)}$, between photon pairs detected by SPD-1 and by another detector (SPD-2) with a known IRF. These functions are related by

$$g^{(2)}(\Delta t) = N(f_1 * f_2)(\Delta t) = N \int f_1(t)f_2(t + \Delta t)dt, \quad (3.4)$$

where f_1 and f_2 are the IRF of SPD-1 and SPD-2 respectively, Δt is the difference in detection time by the two detectors while N is the total number of coincidence events collected from the pair source in the experiment [34].

3.4 Characterizing Timing Jitter of SNSPD

To use SNSPD as a reference detector, we would first need to obtain the IRF and timing jitter of the SNSPD. This is done by obtaining the IRF for SNSPD at 548 nm, 810 nm, and 1550 nm. First, we measure the IRF at 810 nm by obtaining the cross-correlation function $g^{(2)}$ of the photon pairs using the set-up shown in Fig. 3.1. This cross-correlation function, normalized to the background coincidences, is shown in Fig. 3.4.

Since the two detectors are of the same model and operated under the same condition, we can assume that they have the same Gaussian IRF. We can then simplify Eqn. 3.4 to

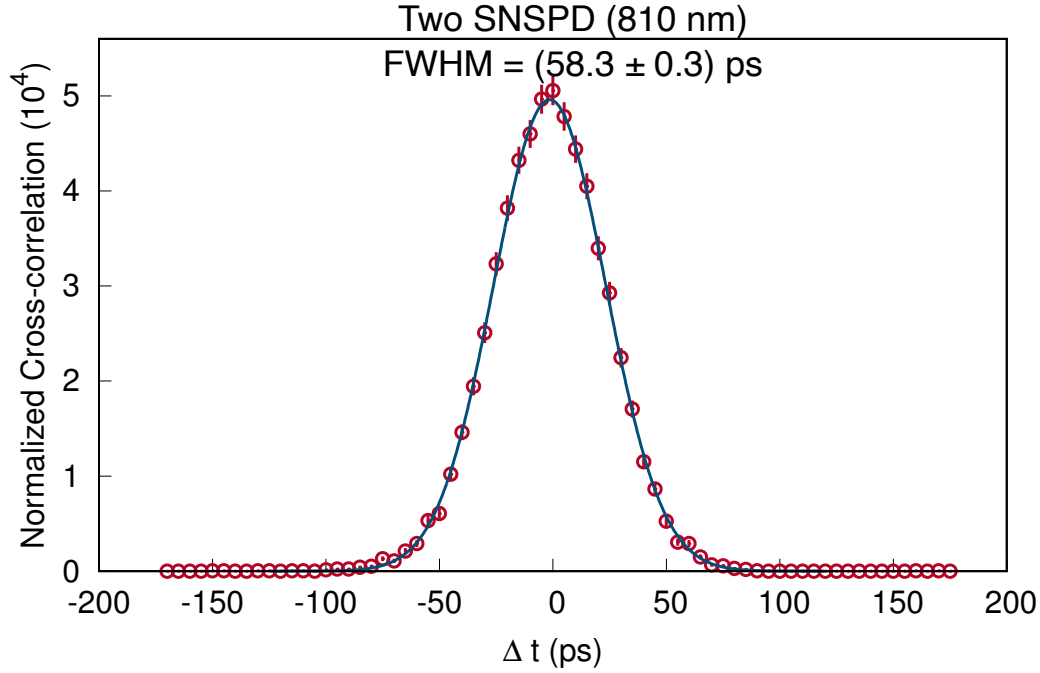


FIG. 3.4. Cross-correlation function between two degenerate 810 nm photon-pairs detected using two SNSPDs. The function is normalized to the background coincidences. Assuming that both detectors are identical, the timing jitter for each detector can be determined to be (39.8 ± 0.1) ps.

$$\begin{aligned} g^{(2)}(\Delta t) &= NG_1(\sigma_1, \Delta t) * G_2(\sigma_2, \Delta t) \\ &= NG(\sigma, \Delta t), \end{aligned} \quad (3.5)$$

where $\sigma = \sqrt{\sigma_1^2 + \sigma_2^2}$, G is a Gaussian distribution with standard deviation σ , while G_1 and G_2 are Gaussian distributions, with standard deviation σ_1 and σ_2 respectively, describing the IRF of each SNSPDs.

From our assumption, we have $\sigma_1 = \sigma_2 = \sigma/\sqrt{2}$. The FWHM of the Gaussian function is related to σ by [35]

$$\text{FWHM} = 2\sqrt{2\ln(2)}\sigma. \quad (3.6)$$

The σ of the Gaussian function in Fig. 3.4 is determined to be 23.9 ps from its FWHM. This means that each SNSPD has a Gaussian IRF with σ_1 and σ_2 of 16.9 ps. Using these σ values, we can then determine the timing jitter of

SNSPD via the FWHM of the IRF.

We determined the timing jitter of SNSPD at 810 nm to be (39.8 ± 0.1) ps. To determine the timing jitter of SNSPD at 1550 nm, we used the photon-pair source shown in Fig. 3.2. The cross-correlation function, normalized to the background coincidences, is shown in Fig. 3.5.

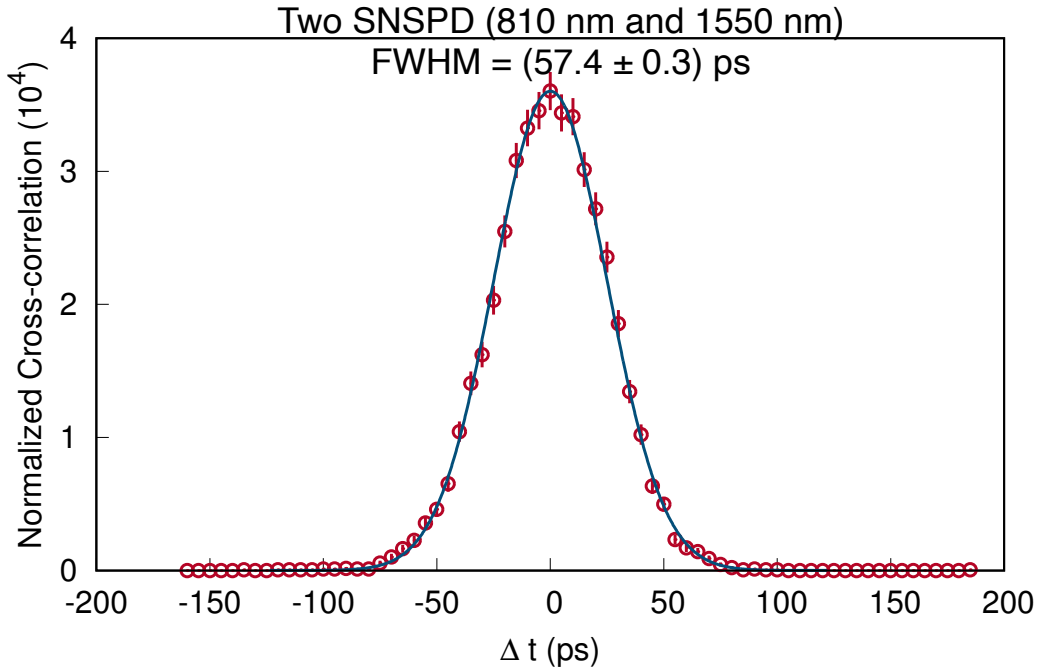


FIG. 3.5. Cross-correlation function between 810 nm and 1550 nm photon-pairs detected using two SNSPDs. The function is normalized to the background coincidences. Assuming that both detectors are identical, the timing jitter for each detector can be determined to be (41.3 ± 0.5) ps.

Using the σ of the SNSPD IRF at 810 nm as σ_1 , we determine the σ of the SNSPD IRF at 1550 nm by designating it σ_2 in Eqn. 3.5. The value of σ of the Gaussian function in Fig. 3.5 is determined to be 25.4 ps from its FWHM. Hence, the value of σ_2 is calculated to be 17.5 ps, and the timing jitter of SNSPD at 1550 nm can be ascertained to be (41.3 ± 0.5) ps from the FWHM of the IRF

Finally, to determine the timing jitter of SNSPD at 548 nm, we use the photon-pair source shown in Fig. 3.3. The cross-correlation function, normalized to the background coincidence, is shown in Fig. 3.6. Using similar calculations as before, we determine the timing jitter of SNSPD at 548

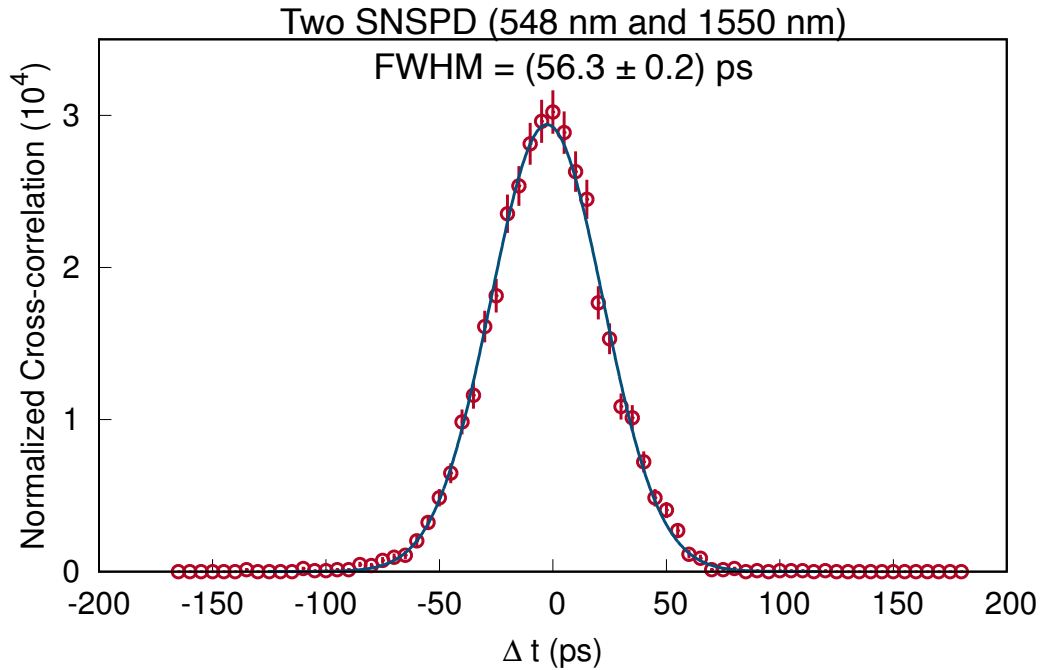


FIG. 3.6. Cross-correlation function between 548 nm and 1550 nm photon-pairs detected using two SNSPDs. The function is normalized to the background coincidences. Assuming that both detectors are identical, the timing jitter for each detector can be determined to be (38.2 ± 0.6) ps.

nm to be (38.2 ± 0.6) ps. The IRF of SNSPD does not change significantly with incident photon wavelength. Besides, it also shows that the timing jitter of SNSPD is relatively constant for photons of different wavelengths, making it a suitable reference detector for our experiment. Therefore, in this report, we designate SNSPD as SPD-2 to obtain the IRF and timing jitter for our SPD of interest, designated as SPD-1.

3.5 Characterizing Timing Jitter of thin SPAD

The timing jitter of our thin SPAD has been previously characterized to be in the order of tens of picoseconds [10]. To properly characterize the timing jitter of thin SPAD, it is crucial that the timing jitter of the reference SPD is comparable or smaller. This is to ensure that the cross-correlation function obtained is not dominated by the IRF of the reference SPD due to its high timing jitter. The low timing jitter of our SNSPD makes it a good

reference detector to characterize the IRF and timing jitter of the thin SPAD. The cross-correlation function obtained using the two detectors is shown in Fig. 3.7

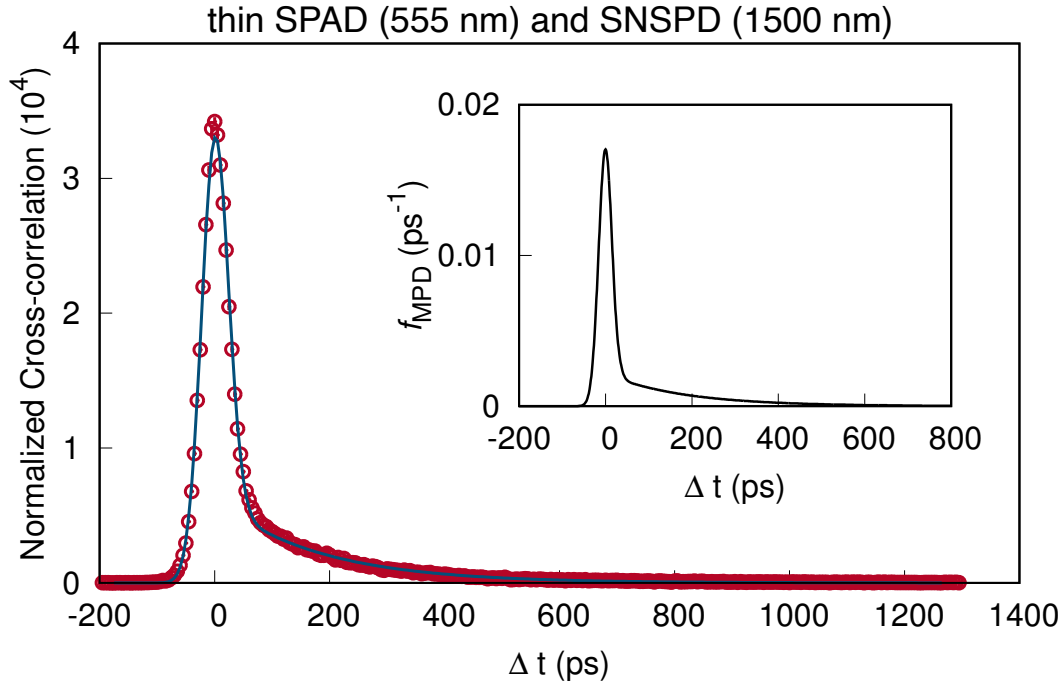


FIG. 3.7. Cross-correlation function between two non-degenerate photon pairs, 555 nm and 1500 nm, detected using thin SPAD and SNSPD respectively. The function is normalized to the background coincidences. The function allows us to extract the IRF of the thin SPAD at 555 nm as shown in the inset. The IRF is approximated to be equal to a linear combination of a Gaussian and exponential function. The time constant τ of the IRF and timing jitter is determined to be (172 ± 2) ps and (38.6 ± 0.9) ps respectively.

From Fig. 3.7, it can be seen that there exist an exponential tail. As it has been previously determined that the IRF of SNSPD is Gaussian, we can thus regard the exponential tail as a feature that is present in the IRF of the thin SPAD.

In the thin SPAD, photoelectrons are typically generated in the depletion region as mentioned previously. The strong electric field that that region allows the electrons to generate secondary electrons, causing an avalanche. In a thin SPAD, its structure gives rise to a finite probability that the photoelectron is generated in the underlying n-substrate instead of the active region. The weaker electric field within this substrate region means

that the photoelectron would slowly drift towards the depletion region where avalanche would occur [36]. This drift of photoelectrons created outside the depletion region might be the reason why an exponential tail is observed in the IRF.

We model the IRF of thin SPAD using a heuristic model, comprising of a linear combination of Gaussian and exponential function [16, 37]. The heuristic model is as follows

$$f_{thin}(\Delta t) = AG(\mu_1, \sigma, \Delta t) + B\theta(\mu_2, \Delta t)e^{-(\Delta t - \mu_2)/\tau}, \quad (3.7)$$

where A and B are the weights of the Gaussian and exponential function respectively. μ_1 and σ are the mean and standard deviation of the Gaussian function. $\theta(\mu_2, \Delta t)$ acts as a step function centered at μ_2 to mark the start of the exponential function with a characteristic time constant τ .

The cross-correlation function, $g^{(2)}(\Delta t)$ between the thin SPAD and SNSPD is obtained from the histogram of the time difference Δt between the detection times of the two detectors. Invoking Eqn. 3.4, we substitute f_1 with Eqn. 3.7 and f_2 with a Gaussian function with approximated FWHM of 41.3 ps (corresponding to SNSPD timing jitter at 1550 nm). The approximation is justified due to the relatively constant SNSPD timing jitter at various wavelengths. This allows us to extract the parameters describing the thin SPAD IRF by fitting the data to the model in Eqn. 3.7. Using the extracted parameters, we can infer the IRF of thin SPAD as presented in Fig. 3.7 (inset).

We determined the time constant τ of the IRF to be (172 ± 2) ps when the photons incident on the thin SPAD is 555 nm. Varying the wavelength of the incident photons causes the value of τ to vary as well. This is presented in Fig. 3.8, where τ can be seen to increase as the wavelength of the photon is increased.

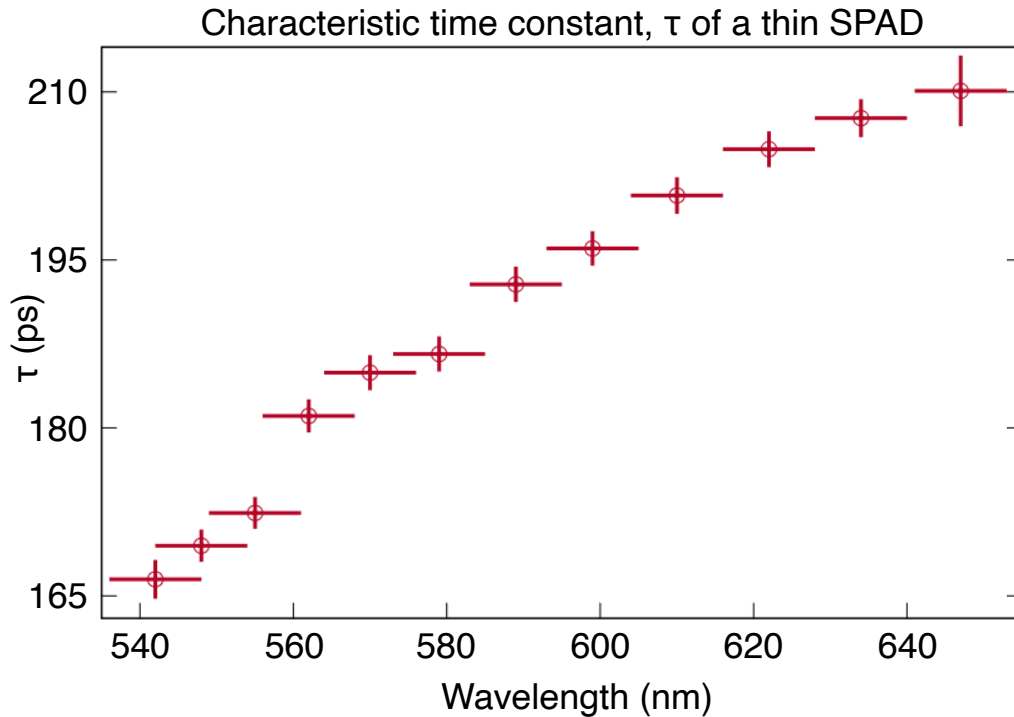


FIG. 3.8. The characteristic time constant of the exponential component in the IRF of a thin SPAD. The time constant increases as incident photon wavelength is increased from 542 nm to 647 nm.

We observed that varying the wavelength of the signal and idler photon (while maintaining pump wavelength) causes some variation in the cross-correlation function, and thus the length of the exponential tail. One explanation for this is that photons with longer wavelength have a greater probability of penetrating deeper and is absorbed further away from the active region of the detector [38, 39]. As a result, more photoelectrons would need to drift towards the depletion region to cause an avalanche. In addition, the deeper penetration means that a longer time is required for the electron to drift towards the depletion region, hence a longer τ is observed. This confirms that the response of a thin SPAD is dependent on the wavelength used in the measurement.

As the IRF of the thin SPAD changes slightly with wavelength, its characterized timing jitter varies correspondingly. This is presented in Fig. 3.9.

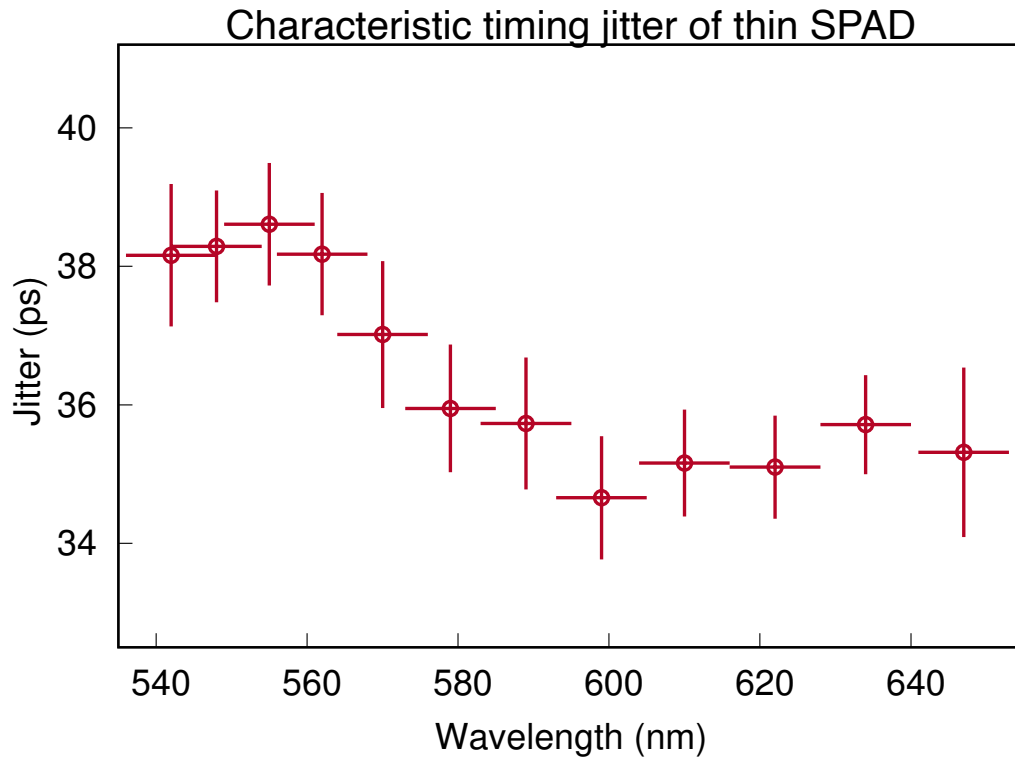


FIG. 3.9. Variation in the characteristic timing jitter of a thin SPAD for different incident photon wavelengths. The characteristic timing jitter varies from 34.7 ps to 38.6 ps for the tested wavelength that ranges from 542 nm to 647 nm.

The characteristic timing jitter of thin SPAD does not seem to vary much as seen in Fig. 3.9. One reason for this is that despite the slight change in IRF, the changes mainly occur in the exponential tail. As a result, the FWHM of the IRF which gives a measure of the timing jitter is relatively unaffected. The measured FWHM could have stayed relatively unchanged due to photons absorption in the active region remains unaffected by the change in wavelength. Thus, the thin SPAD has a relatively stable timing jitter across different wavelengths. Nevertheless, the existence of the exponential tail and slight variation in IRF with wavelength means that there is a need to characterize the IRF of a thin SPAD at the desired wavelength since the change in the exponential tail will affect the accuracy of a time-resolved measurement.

3.6 Characterizing Timing Jitter of InGaAs SPAD

Other than thin SPAD, we also characterize the IRF and timing jitter of an InGaAs SPAD, a detector widely used in quantum communication to detect photons at telecommunications band (1100 nm - 1600 nm). The cross-correlation function obtained using SNSPD and InGaAs SPAD, normalized to the background coincidences, is presented in Fig. 3.10.

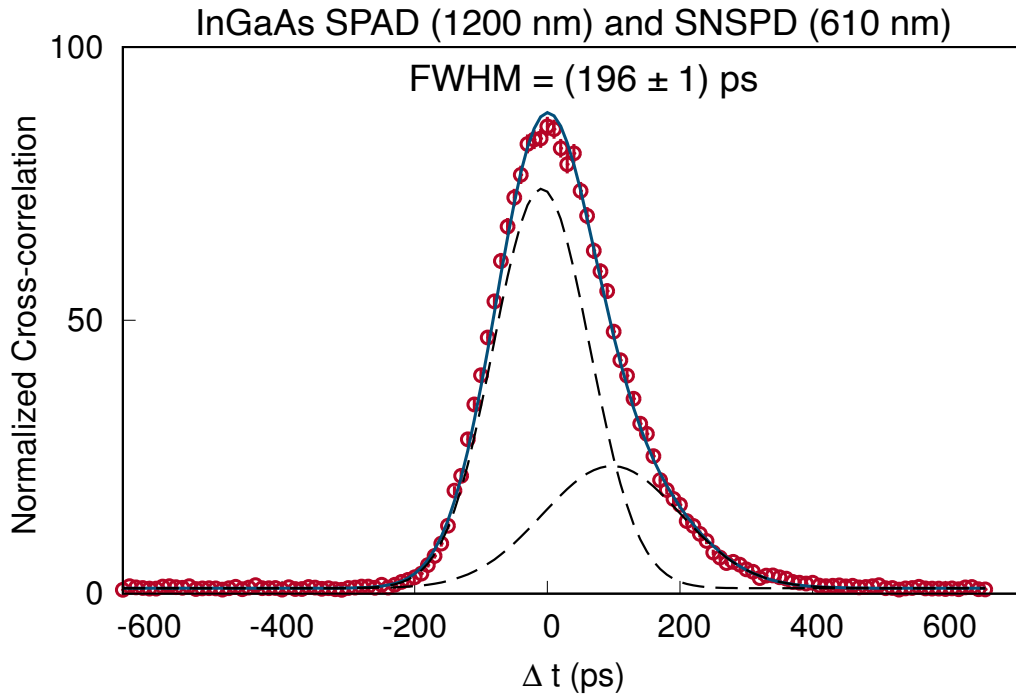


FIG. 3.10. Cross-correlation function between two non-degenerate photon pairs, 1200 nm and 610 nm, detected using InGaAs SPAD and SNSPD respectively. The function is normalized to the background coincidences. As the SNSPD is much faster than InGaAs SPAD, this function can be approximated to be the IRF of InGaAs SPAD at 1200 nm. The function was approximated to be a linear combination of two Gaussian functions, with a FWHM of (196 ± 1) ps [40].

Using a similar approach to when we characterize the IRF of thin SPAD, we characterize the IRF of an InGaAs SPAD by measuring the cross-correlation function due to the detection of photons by the InGaAs SPAD and SNSPD. However, as the timing jitter of an InGaAs SPAD is expected to be significantly larger than that of an SNSPD, the

cross-correlation function obtained can be used as an approximation for the IRF of the InGaAs SPAD [40, 41].

We approximate the IRF of the InGaAs SPAD with a heuristic model comprising of a linear combination of two Gaussian functions [40].

$$f_{InGaAs}(\Delta t) \approx g^{(2)}(\Delta t) = AG(\mu_1, \sigma_1, \Delta t) + BG(\mu_2, \sigma_2, \Delta t), \quad (3.8)$$

where A and B are the weights of each Gaussian function and the subscripts on the μ 's and σ 's denote the mean and standard deviation of the respective Gaussian functions.

The two Gaussian functions in the IRF of InGaAs SPAD are due to the higher breakdown voltage at the edge of the SPAD device as compared to the breakdown voltage at the central active area [40]. This results in slower detection of photons that originate near the edge of the device as compared to those generated at the central active area. Hence, the IRF of InGaAs SPAD comprises of two peaks.

The characterized timing jitters from the FWHM of the IRF are presented in Fig. 3.11

Varying the wavelength of the photon incident on the InGaAs SPAD (1200 nm - 1600 nm), we observed that there is no significant change in the detector IRF and timing jitter. The timing jitter is determined to be around 196 ps to 198 ps. This might be because the timing jitter in an InGaAs SPAD is mainly contributed by the variation in the build-up of the avalanche process in the active area, which is independent of wavelength [42, 43].

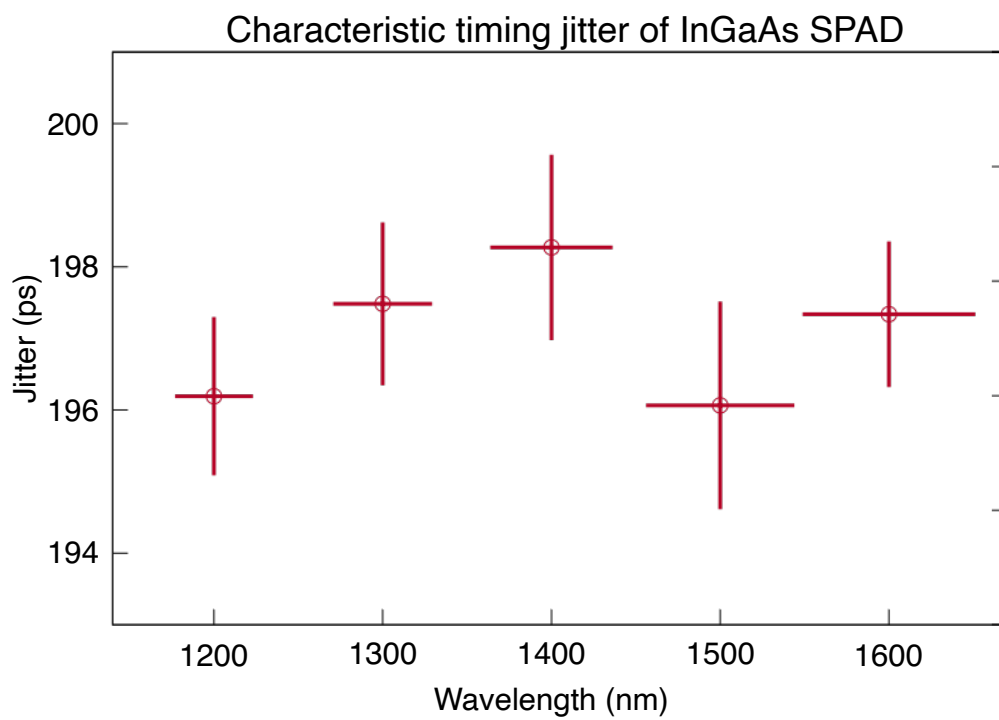


FIG. 3.11. Characteristic timing jitter of an InGaAs SPAD for different incident photon wavelengths. The timing jitter varies from 196 ps to 198 ps for the tested wavelength that ranges from 1200 nm to 1600 nm.

Chapter 4

Conclusion

In this report, the IRF and timing jitter of three different detectors have been characterized. We measured that the timing jitter of our SNSPD around 40 ps at 548 nm, 810 nm, and 1550 nm. Furthermore, we also demonstrated a technique for characterizing the IRF and timing jitter of a thin silicon SPAD and InGaAs SPAD using the SNSPD as a reference detector.

We experimentally demonstrated the wavelength-tunability of our SPDC source over the visible and telecommunications band, exhibiting a comparable tunability to the existing femtosecond pulsed laser systems. We successfully characterized the IRF and timing jitter of a thin silicon SPAD from wavelengths 542 nm to 647 nm. The timing jitter is determined to be approximately constant around 35 ps to 38 ps while the IRF is observed to have an exponential tail, which changes with the incident photon wavelength. Using incident photons with higher wavelength cause time constant, τ , of the exponential tail to increase. The subsequent characterization of the IRF and timing jitter of an InGaAs SPAD from 1200 nm to 1600 nm shows that both the IRF and timing jitter are independent of the incident photon wavelength. The timing jitter of InGaAs SPAD is determined to be around 196 ps to 198 ps

Our experiment showed that the IRF of the thin silicon SPAD are dependent on the wavelength of the photons used. Existing characteristics provided by the manufacturer can provide a rough approximation for the detector characteristics but is inadequate to get an accurate measurement. This implies that precision measurements such as measuring the photon statistics of narrowband astronomical sources and characterizing fluorescent markers at different wavelengths require prior characterization of the detector IRF and timing jitter at the required wavelengths [3, 16].

Bibliography

- ¹J. Zhang, M. A. Itzler, H. Zbinden, and J.-W. Pan, “Advances in InGaAs/InP single-photon detector systems for quantum communication”, *Light: Science & Applications* **4**, e286–e286 (2015).
- ²R. H. Hadfield, “Single-photon detectors for optical quantum information applications”, en, *Nature Photonics* **3**, 696–705 (2009).
- ³S. Cova, A. Longoni, and A. Andreoni, “A semiconductor detector for measuring ultraweak fluorescence decays with 70 ps FWHM resolution”, *Quantum Electronics, IEEE Journal of* **19**, 630–634 (1983).
- ⁴C. Niclass, A. Rochas, P.-A. Besse, and E. Charbon, “Design and characterization of a CMOS 3-D image sensor based on single photon avalanche diodes”, *IEEE Journal of Solid-State Circuits* **40**, 1847–1854 (2005).
- ⁵W. R. Bosenberg, L. K. Cheng, and C. L. Tang, “Ultraviolet optical parametric oscillation in *B*-BaB₂O₄”, *Applied Physics Letters* **54**, 13–15 (1989).
- ⁶D. Renker, “Photosensors”, *Nuclear Instruments and Methods in Physics Research Section A: Accelerators, Spectrometers, Detectors and Associated Equipment*, 15–20 (2004).
- ⁷M. Richmond, *Einstein and the Photoelectric effect*, <http://spiff.rit.edu/classes/phys314/lectures/photoe/photoe.html>.

- ⁸Hamamatsu Photonics K. K, “Photomultiplier Tubes Basics and Applications”, en, 323 (2007).
- ⁹D Renker and E Lorenz, “Advances in solid state photon detectors”, en, Journal of Instrumentation **4**, P04004–P04004 (2009).
- ¹⁰A. Giudice, M. Ghioni, R. Biasi, F. Zappa, S. Cova, P. Maccagnani, and A. Gulinatti, “High-rate photon counting and picosecond timing with silicon-SPAD based compact detector modules”, en, Journal of Modern Optics **54**, 225–237 (2007).
- ¹¹A. Gulinatti, I. Rech, P. Maccagnani, M. Ghioni, and S. Cova, “Improving the performance of silicon single-photon avalanche diodes”, in Proc.SPIE, Vol. 8033 (May 2011).
- ¹²C. M. Natarajan, M. G. Tanner, and R. H. Hadfield, “Superconducting nanowire single-photon detectors: physics and applications”, en, Superconductor Science and Technology **25**, 063001 (2012).
- ¹³G. N. Gol’tsman, O. Okunev, G. Chulkova, A. Lipatov, A. Semenov, K. Smirnov, B. Voronov, A. Dzardanov, C. Williams, and R. Sobolewski, “Picosecond superconducting single-photon optical detector”, en, Applied Physics Letters **79**, 705–707 (2001).
- ¹⁴J. K. W. Yang, A. J. Kerman, E. A. Dauler, V. Anant, K. M. Rosfjord, and K. K. Berggren, “Modeling the Electrical and Thermal Response of Superconducting Nanowire Single-Photon Detectors”, IEEE Transactions on Applied Superconductivity **17**, 581–585 (2007).
- ¹⁵Single Quantum, *Single Quantum Eos - SNSPD Closed-Cycle System*, 2019.
- ¹⁶P. K. Tan, A. H. Chan, and C. Kurtsiefer, “Optical intensity interferometry through atmospheric turbulence”, Monthly Notices of the Royal Astronomical Society **457**, 4291–4295 (2016).

- ¹⁷B. Baek, K. S. McKay, M. J. Stevens, J. Kim, H. H. Hogue, and S. W. Nam, “Single-photon detection timing jitter in a visible light photon counter”, *IEEE Journal of Quantum Electronics* **46**, 991–995 (2010).
- ¹⁸J. Lee, L. Shen, A. Cerè, J. Troupe, A. Lamas-Linares, and C. Kurtsiefer, “Symmetrical clock synchronization with time-correlated photon pairs”, *Applied Physics Letters* **114**, 101102 (2019).
- ¹⁹P. K. Tan and C. Kurtsiefer, “Temporal intensity interferometry for characterization of very narrow spectral lines”, *Monthly Notices of the Royal Astronomical Society* **469**, 1617–1621 (2017).
- ²⁰C. K. Hong, Z. Y. Ou, and L. Mandel, “Measurement of subpicosecond time intervals between two photons by interference”, *Physical Review Letters* **59**, 2044–2046 (1987).
- ²¹W. H. Louisell, A. Yariv, and A. E. Siegman, “Quantum fluctuations and noise in parametric processes. I.”, *Physical Review* **124**, 1646 (1961).
- ²²M. H. Rubin, D. N. Klyshko, Y. H. Shih, and A. V. Sergienko, “Theory of two-photon entanglement in type-II optical parametric down-conversion”, *Physical Review A* **50**, 5122–5133 (1994).
- ²³P. G. Kwiat, K. Mattle, H. Weinfurter, A. Zeilinger, A. V. Sergienko, and Y. Shih, “New High-Intensity Source of Polarization-Entangled Photon Pairs”, *Physical Review Letters* **75**, 4337–4341 (1995).
- ²⁴C. Kurtsiefer, M. Oberparleiter, and H. Weinfurter, “Generation of correlated photon pairs in type-II parametric down conversion—revisited”, *Journal of Modern Optics* **48**, 1997–2007 (2001).
- ²⁵L. Shen, J. Lee, L. P. Thinh, J.-D. Bancal, A. Cerè, A. Lamas-Linares, A. Lita, T. Gerrits, S. W. Nam, V. Scarani, and C. Kurtsiefer, “Randomness Extraction from Bell Violation with Continuous Parametric Down-Conversion”, *Physical Review Letters* **121**, 150402 (2018).

- ²⁶P. A. Franken and J. F. Ward, "Optical Harmonics and Nonlinear Phenomena", *Reviews of Modern Physics* **35**, 23–39 (1963).
- ²⁷John C Jacco, "KTiOPO₄ (KTP) Past, Present, And Future", in *Proc.SPIE*, Vol. 0968 (Jan. 1989).
- ²⁸M. M. Fejer, G. A. Magel, D. H. Jundt, and R. L. Byer, "Quasi-phase-matched second harmonic generation: tuning and tolerances", *IEEE Journal of Quantum Electronics* **28**, 2631–2654 (1992).
- ²⁹D. Eimerl, L. Davis, S. Velsko, E. K. Graham, and A. Zalkin, "Optical, mechanical, and thermal properties of barium borate", *Journal of Applied Physics* **62**, 1968–1983 (1987).
- ³⁰D. N. Nikogosyan, *Nonlinear Optical Crystals: A Complete Survey* (Springer New York, 2006).
- ³¹Shibuya Optical, *Multi Band Filter (Wavelength Calibration Filter)*, 2014.
- ³²F. J. Duarte, P. Kelley, L. W. Hillman, and P. F. Liao, *Dye laser principles: with applications* (Academic Press, 1990).
- ³³E. Sorokin, S. Naumov, and I. T. Sorokina, "Ultrabroadband infrared solid-state lasers", *IEEE Journal of Selected Topics in Quantum Electronics* **11**, 690–712 (May-June 2005).
- ³⁴A. Papoulis, "The Fourier integral and its applications", Polytechnic Institute of Brooklyn, McCraw-Hill Book Company Inc., USA, ISBN: 67-048447-3 (1962).
- ³⁵E. W. Weisstein, *Gaussian Function*, en, <https://mathworld.wolfram.com/GaussianFunction.html>, Text.
- ³⁶A. Lacaita, M. Ghioni, and S. Cova, "Double epitaxy improves single-photon avalanche diode performance", *Electronics Letters* **25**, 841–843 (1989).

- ³⁷Q. Hernandez, D. Gutierrez, and A. Jarabo, "A computational model of a single-photon avalanche diode sensor for transient imaging", arXiv preprint arXiv:1703.02635 (2017).
- ³⁸S. Cova, G. Ripamonti, and A. Lacaita, "Avalanche semiconductor detector for single optical photons with a time resolution of 60 ps", en, *Nuclear Instruments and Methods in Physics Research Section A: Accelerators, Spectrometers, Detectors and Associated Equipment* **253**, 482–487 (1987).
- ³⁹M. A. Green and M. J. Keevers, "Optical properties of intrinsic silicon at 300 K", *Progress in Photovoltaics: Research and Applications* **3**, 189–192 (1995).
- ⁴⁰A. Tosi, F. Acerbi, A. Dalla Mora, M. A. Itzler, and X. Jiang, "Active Area Uniformity of InGaAs/InP Single-Photon Avalanche Diodes", *IEEE Photonics Journal* **3**, 31–41 (2011).
- ⁴¹T. Lunghi, C. Barreiro, O. Guinnard, R. Houlmann, X. Jiang, M. A. Itzler, and H. Zbinden, "Free Running Single Photon Detection based on a negative feedback InGaAs APD", *Journal of Modern Optics* **59**, 1481–1488 (2012).
- ⁴²S. Margalit and A. Yariv, "Chapter 2 Integrated Electronic and Photonic Devices", in *Semiconductors and Semimetals*, Vol. 22, edited by W. Tsang (Elsevier, Jan. 1985), pp. 203–263.
- ⁴³M. A. Itzler, r. Ben-Michael, C. F. Hsu, K. Slomkowski, A. Tosi, S. Cova, F. Zappa, and R. Ispasoiu, "Single photon avalanche diodes (SPADs) for 1.5 μm photon counting applications", *Journal of Modern Optics* **54**, 283–304 (2007).